

Detection and quantification of pore, solid and gravel spaces in CT images of a 3D soil sample

B. Ojeda-Magaña^{a*}, R. Ruelas^a, J. Quintanilla-Domínguez^b, J. G. Robledo-Hernández^a, C.J. Sturrock^c, S.J. Mooney^c, A.M. Tarquis^{d,e}

^a*Departamento de Ingeniería de Proyectos, Universidad de Guadalajara, José Guadalupe Zuno No. 48, C.P. 45150, Zapopan, Jal., México.*

^b*Departamento de Ingeniería en Redes y Telecomunicaciones, Universidad Politécnica de Juventino Rosas, Hidalgo No. 102, Comunidad de Valencia, C.P. 38253, Santa Cruz de Juventino Rosas, Gto., México.*

^c*School of Biosciences, University of Nottingham, Sutton Bonington Campus, Loughborough, Leicestershire, LE12 5RD, UK.*

^d*GSC & CEIGRAM, ETSIAAB, Universidad Politécnica de Madrid (UPM). Ciudad Universitaria, sn. C.P. 28040, Madrid, España.*

Abstract

In this study, we scanned the core of a cylindrical a soil sample (60mm diameter and 100mm height) by X-ray Computed Tomography (CT) producing 300 consecutive 2D digital images with 16-bit gray level depth and a resolution of 32 microns (image size 676×676 pixels). The aim of this work was to determine the geometry and spatial distribution of the elements in a sample, related in this case to pore, solid and gravel, inside each 2D image for the latter reconstruction of the corresponding 3D approximation of the elements using the total set of 300 soil images. Therefore, it was possible to determine the relative percentage of each element present in each 2D image and, correspondingly, the structure and total percentage in the 3D reconstruction. The

identification of elements in the 2D image slices was very well accomplished using three standard segmentation algorithms: k-Means, Fuzzy c-Means and Otsu multilevel. In order to compare and evaluate the quality of results, a non-uniformity (NU) measure was applied such that low values were indicative of homogeneous regions. Due to the depth of the greyscale of the images, the results were very similar with comparable statistics and homogeneity (NU values) among the detected materials of the three algorithms. That suggests that the pore, solid and gravel spaces were very well identified, and this is reflected through their connectivity in the 3D reconstruction. Additionally, the gray level depth was reduced to 8 bits and the same study was undertaken. In this case, the quality of results was comparable to the previous ones, as the number of elements and NU values were very close. However, this also depends largely on the high resolution of the images. Thereby, the soil sample of this work was very well characterized using the simplest and most common algorithms for image segmentation thanks to the high contrast and resolution, and regardless the depth of the grey-level.

Keywords: 3D soil image analysis, X-Ray CT, Realistic 3-D reconstruction, Porosity, Images segmentation.

1. Introduction

The best description of soils can only be possible when their elements are clearly identified, quantified and the structure of the soil is well established. This is a requirement for the functional analysis of a soil sample based, for

instance, on the physical, chemical or biological processes that could happen in its structure [1], [2], [3], [4], [5], [6], [7]. In most of the reported studies the main interest has been the soil pores; looking at their geometry, spatial distribution and connectivity, which can be evaluated through the three-dimensional (3D) volume reconstruction of the sample. However, as the technology advances, there is a growing interest for the identification of more discrete elements, such as the soil solid space including primary particles of varying sizes (e.g. sand grains and gravel).

Nowadays, and due to the available technology, the most preferred approach for the analysis of soils is to use non-intrusive methods based on X-ray imaging, such that the soil samples are not altered after removal from the field. Computed Tomography (CT) offers an attractive opportunity for 3D insight of the inner structure of objects and materials, and it is an interesting alternative as a set of two-dimensional greyscale image slices (2D) of high resolution (μ CT) can be sequentially produced throughout the complete 3D soil samples [8]. The resolution of the images depends on the quality of the scan, as well as on the depth of the grey-level that is normally represented by 8 or 16 bits (high quality of medical images). In this case of study, a set of 300 2D image slices in TIFF format, with a resolution of 32 microns, an image size of 676×676 pixels and 16 bit grey values, were extracted from an undisturbed soil sample.

The problem posed in this work has to be with the identification of discrete materials in a soil sample: solid, gravel and pore of each 2D CT image into

three objects or elements; pores, solids and gravel, in order to quantify them and determine the internal structure of the soil sample. Once the material and pores had been identified, they were individually represented in binary images for quantification. With these results, it was then possible to undertake 3D reconstruction of the soil sample and its elements, as shown in the results section.

The grey level of the pixels is the only feature used here as the main information into the 2D CT soil images in order to recognize the different materials and pore spaces in the soil sample. This explains why most of these studies are based on segmentation methods [9], [10], [11], [12], where a threshold value can be established such that pixels with values greater than this threshold are related to a material or to a pore space, or vice versa, depending which group is being analyzed [13], [14], [15]. One of the most popular methods to find automatically the threshold is the Otsu method, which allows finding n discrete groups or materials within an image [16], [17]. Among the different approaches for the detection of objects in 2D soil images are manual methods, which are realized by an expert or a group of experts who establish the edge of regions of interest. However, this can be an extremely challenging task due to the shape and quantity of pores and solids or any type of materials present inside a soil sample. In these circumstances, a more attractive approach is an automatic method that estimates the thresholds of grey levels to detect the different objects. The methods used in this work were the k-Means [18] and Fuzzy c-Means (FCM) [19] clustering algorithms, as segmentation methods,

as well as the Otsu algorithm as a multilevel thresholding method [5]. All these methods were applied directly to the original CT images (i.e. they were not preprocessed, which is an advantage, as a partial loss of information of interest is avoided due to this process).

The main challenge for this kind of problems is to find the “ideal borders” between the elements or segments present within the images. Unfortunately, or luckily, dozens of methods have been developed that could be used to detect the elements in a CT soil image. However, each method has its own advantages and limitations, where a particular method was developed in order to overcome the deficiencies of the others. Consequently, the solution depends on the characteristics of each application, as well as on the type and quality of the scanner for the image acquisitions, the contrast between the grey levels, the noise, the resolution, the depth of the pixels (8, 12 or 16 bits), among others. That is, a solution is always related to the particularities of the set of CT images of the study. That is to say, the model has to be adapted for different sets of images. Besides, the images with manual segmentation (ground truth) are rarely available for the algorithms validation.

As the technology evolves and the quality of the CT images improves, the defy is to better characterize the complex structure of the soils. This requires detecting, not only the solid-void spaces, but also other elements that could help to reach a more accurate description of the soil, allowing a better modelling and understanding of its complexity, what is intended in this work.

Therefore, the main goal of this work is the detection and quantification of solid, gravel and solid-void in real soil CT scan images. In this work, we use three standard algorithms; k-Means, Fuzzy c-Means and Otsu multilevel, as the results are of great quality for the soil sample studied and the quality of images available. Besides, the depth representation of grey levels was reduced from 16 to 8 bits, and the same tests were realized in order to evaluate if the quality of results could be maintained or if there was loss of information. According to results, it was possible to verify that this was the case and the results remained practically unchanged except for the slight differences in micro and medium pores for the two different levels of depth. Namely, the size, the shape, the homogeneity and the number of elements had a high degree of agreement. The number of elements was determined directly from the segmentation results, the size by the number of pixels of each object, the shape by a comparative analysis of results among the different methods, as well as the continuity between two consecutive 2D images. Additionally, a 3D reconstruction by element identified was made from the binary images for the 16 and 8 bits depth. Finally, the homogeneity, or the degree of uniformity, was calculated using a NU measure applied to each particular region, object or group. Both final comments reinforce the quality of the results.

This document is structured as follows. Section 2 contains the features of a soil sample, the set of 300-2D real images used in this study, the reduction from 16 to 8 bits grey level depth, the image segmentation algorithms, the Non-Uniformity measure and the procedure applied for the detection and

quantification of the main elements in the images. Section 3 provides the segmentation results when applying three standard methods, the quantities of elements in each CT image, the NU values per each 2D soil image, and the 3D reconstruction using the 300-2D binary images of the dataset. Besides, this section includes a comparison and discussion about the results and according to the different segmentation methods, the homogeneity of the elements represented by the NU values, the resulting 3D CT soil images and a comparative analysis between the results with 16 and 8 bits. Finally, section 4 contains the main conclusions of this work.

2. Materials and methods

2.1. Study area and soil sampling

In this work, an intact soil sample (60mm diameter and 100mm height) was collected from *La Herreria* located in the low land mountain area of *Sierra de Guadarrama* [20]. It represents a highly degraded type of site as a result of the livestock keeping. Soil sample was extracted from the first layer (Horizon A) being the result of biological alteration with roots resulting in fertile soil. This layer is moderately acid, with 2% of organic matter, 0.8% of Fe_2O_3 and sandy texture [21].

X-ray CT scanning was performed using a Phoenix v|tome|x m 240 kV system (GE Sensing & Inspection Technologies GmbH, Wunstorf, Germany) at the Hounsfield Facility, University of Nottingham, UK. The scanner consisted of a 240kV microfocus X-ray tube fitted with a tungsten reflection

target and a DXR 250 digital detector array with $200 \mu\text{m}$ pixel size (GE Sensing & Inspection Technologies GmbH, Wunstorf, Germany). A maximum X-ray energy of 140kV and $200 \mu\text{A}$ was used to scan the soil core. A total of 2400 projection images were acquired over a 360° rotation. Each projection was the average of six images acquired with a detector exposure time of 200 ms and the resulting isotropic voxel edge length was $32 \mu\text{m}$. Reconstruction of the projection images to produce three-dimensional (3D) volumetric data set was performed using the software `datos|rec` (GE Sensing & Inspection Technologies GmbH). The reconstructed CT volume was visualized and quantified using VG StudioMAX $\text{\textcircled{R}}2.2$ (Volume Graphics GmbH, Heidelberg, Germany). The algorithms used in this work were implemented in Matlab running in a PC at 2.6 GHz with a processor Intel Xeon ES-2640 v3 CPU and 16 GB of RAM.

The 3D image of the soil sample used in this work is represented by $676 \times 676 \times 300$ voxels; Fig. 1 shows a complete 3D image of the soil sample. From this sample, 300 slices were made through 2D CT images with a resolution of 676×676 pixels, and a grey level depth of 16 bits. The 2D original images were in *.TIFF format and Fig. 2 shows some of them.

2.2. Reduction from 16 to 8 bits in the grey depth level

As most of the images in digital image processing hitherto are given in 8 bits, the grey level depth of the images of this work were changed from 16 to 8 bits. The objective was to evaluate if a decrease in number of grey values

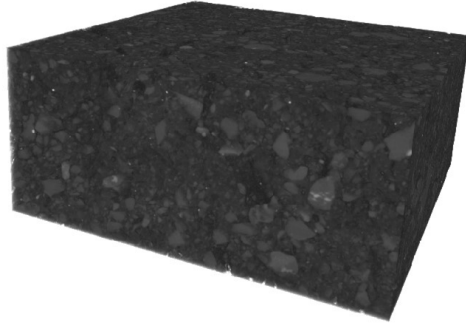


Figure 1: 3D representation of the soil sample.

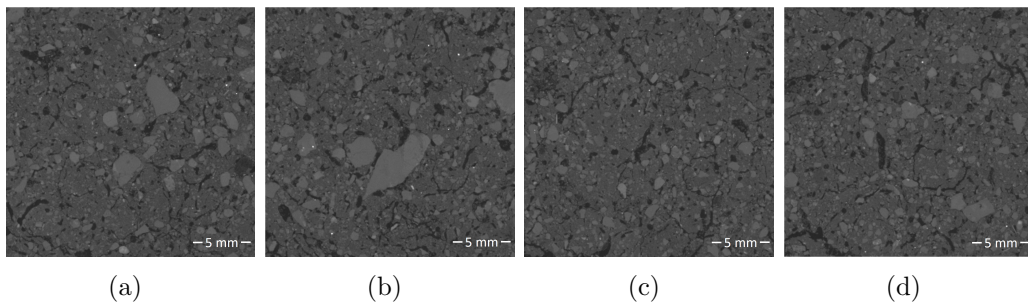


Figure 2: Four examples of 2D original images of the soil sample. a) Im_000, b) Im_001, c) Im_002 and d) Im_299.

influenced the quality of segmentation results. Hence, the grey values were changed simply by dividing the grey level of each pixel by 2^8 , and rounding when necessary.

2.3. Algorithms for the segmentation of images

A 2D image is defined in the $X_1 \times X_2$ bi-dimensional space where there is a grey level, in most of the cases, in others it could be any color space, associated to each position or pixel. These grey values can be considered as a third dimension L such that the images are defined in $X_1 \times X_2 \times L$, knowing that X_1 and X_2 depend on the spatial resolution of each image and are

generally given in pixels more than in dimensional magnitudes, whereas L depends on the grey value depth of the image that is commonly represented by 2^8 or 2^{16} integer grey values. Therefore, representing an image by the set of pixels ($P_1 \times P_2$) we get a three-dimensional discrete space defined in $P_1 \times P_2 \times L$, where $P_1 \times P_2$ represents the image size. In this case the pixels have a constant base ($p_1 \times p_2$) and a variable height that depends on the grey value, a value in the $[0, (2^{16} - 1)]$ interval for 16 bits depth for example.

Now, when there is only one object and the background in an image, both elements in the $P_1 \times P_2 \times L$ space, they are represented by different grey values. For example, in Fig. 3a there is a simple image of $1 \times 2 \times 2^8$. In this case, the recognition of one object from the other is realized by identifying a point of separation of objects (pso), or a level, to separate the height of the space in two groups, as shown in Fig. 3c, one with the darker grey levels (usually the background and illustrated as Object 1 in the Fig. 3c) and the other with the lighter grey levels (the object of interest or Object 2 in Fig. 3c). A similar situation happens when there are more than two objects in an image; the grey scale, or the height of the space, has to be divided according to the number of objects to identify. See Fig. 3b and 3d for the case of four objects. The segmentation methods are used to determine the pso as in the examples of Fig. 3. In a real image the pixels of an object could be a space not totally connected. This is the case for the pores in the soil images where they appear as isolated objects in the 2D or 3D images [22].

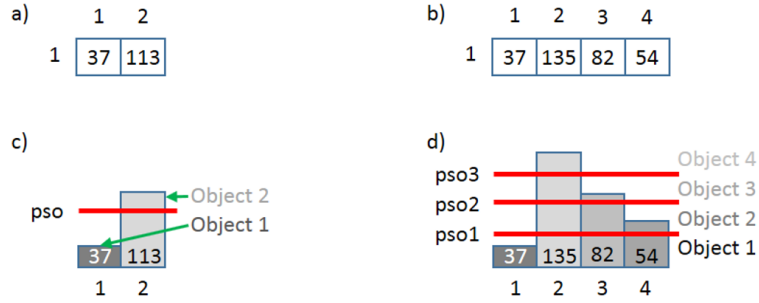


Figure 3: Two simple images and identification of objects by division of the L dimension. a) Image of $1 \times 2 \times 2^8$, b) Image of $1 \times 4 \times 2^8$ c) Identification of two objects, d) Identification of four objects.

If the images are defined in $X_1 \times X_2 \times L$, the segmentation process can be interpreted as a function that transforms this space into another simpler, that is,

$$f : X_1 \times X_2 \times L \rightarrow X_1 \times X_2 \times l \quad (1)$$

where X_1 and X_2 represent two spatial dimensions, L the grey scale and l a reduced set of clusters or groups, that is, $l = 0,65535$ for $L = 2^{16}$. See Fig. 4 where each group is related to a range of grey values, that is, $g_i \subset [0, 65535]$ for 16 bits and $i = 1, \dots, c$. The total range of the groups did not necessarily represent the totality of the grey scale and it depends strongly on the application and on each particular image. Therefore, at the end all the grey values within a group g_i are associated to one particular object. The elements of a particular object can be set white and the rest of elements of the image in

black in order to evaluate each object in an isolated way. The result, in this case, is a binary image. However, the elements of each segmented object can be attributed to a different color such that all the objects can be viewed and evaluated at the same time.

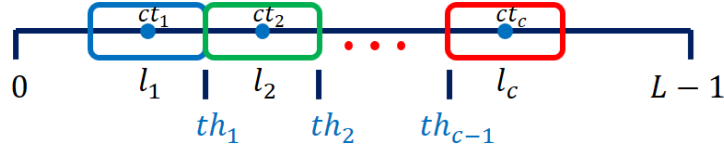


Figure 4: Greyscale values for L equal to 2^8 or 2^{16} for 8 or 16 bits respectively.

Two basic principles for image segmentation consist of calculating the centers or prototypes of the groups (represented by ct_i in Fig. 4) and the elements around them to form the different groups or clusters. On the other hand, the other principle is based on the calculus of thresholds (represented by th_i in Fig. 4) that establish the limits among the groups. The first principle is very well implemented by clustering methods with the k-Means and the Fuzzy c-Means (FCM) the most popular algorithms, whereas the second principle is implemented by multilevel thresholding methods, where Otsu's method is the most commonly used. These clustering and multilevel thresholding methods were used in this work to detect pores, solids and gravel in CT soil sample images and are described in the following sub-sections.

Both clustering algorithms, k-Means and FCM, are convergent although they always find a local minimum and there is no possibility to know if a given solution is, in fact, the global minimum. In fact, the initial state has a great

influence on the solution. Therefore, the common practice is to execute them repeatedly although each time using a new random initial condition[23] to retain the solution with the smallest criterion value. The drawbacks of these algorithms are the effect of noise, overlapping clusters and the increasing dimensionality. Fig. 5 shows an example on the procedure using these methods.

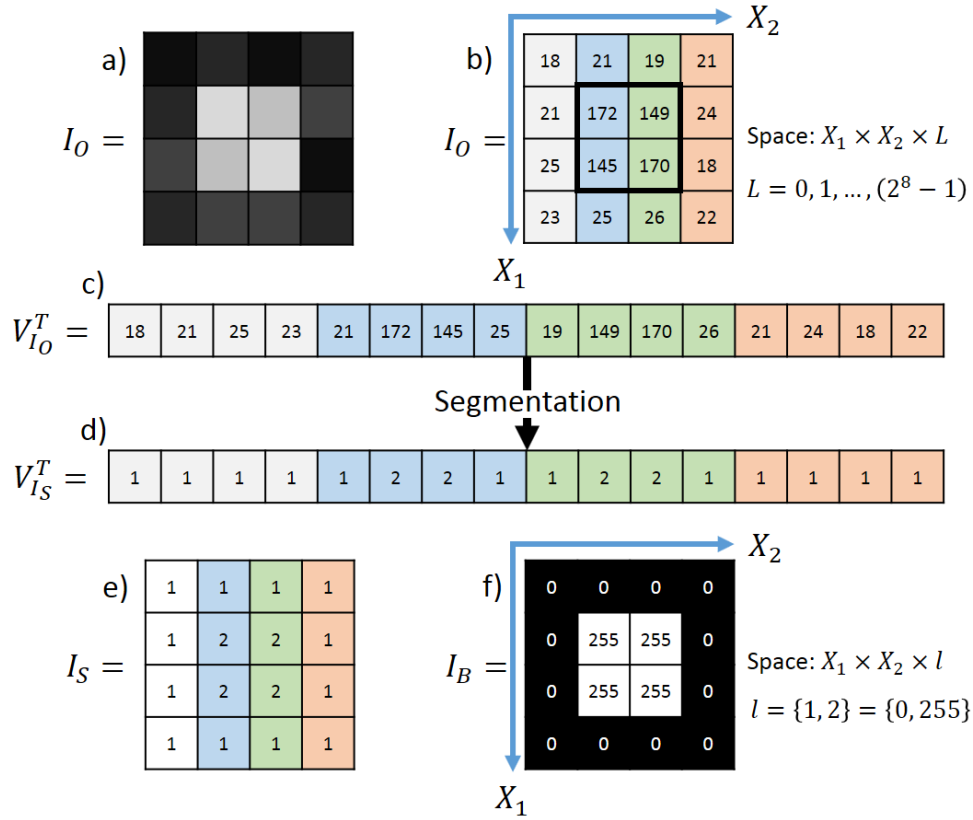


Figure 5: Segmentation of a digital image for clustering algorithm in the greyscale for 8 bits. a) Original image I_O , b) original image I_O represented with the grey values in L , c) array as a transpose vector $V_{I_O}^T$ of the original image for image processing, d) segmentation (by clustering) results as a transpose vector $V_{I_S}^T$ in two clusters or regions, e) segmented image I_S and f) binary image I_B .

The k-Means algorithm allows the identification of k clusters through a representative element given like a center, mean value or a prototype μ_h of each cluster. The initial μ_h are established randomly and a distance is calculated between them and each data point x_i , so that each data point is assigned to the cluster with the nearest center. Once all the data points were redistributed, the centers or mean values are recalculated. That is,

$$\mu_h^{(k)} = \frac{\sum_{x \in X_h} p(x)x}{\sum_{x \in X_h} p(x)}, \quad h = 1, 2, \dots, k \quad (2)$$

and stops when one of the following criteria is satisfied,

- If $J_h = \min_{\{\mu_1, \mu_2, \dots, \mu_k\}} \sum_{h=1} \sum_{x \in X_h} \|x - \mu_h\|^2 < \varepsilon$, then stop, or
- If $\|\mu_h^{(k)} - \mu_h^{(k-1)}\| < \varepsilon$ then stop.

This algorithm is sensitive to initial conditions and can be affected by the variation of size in clusters, shapes, densities and outliers. In fact, if the method is based on the Euclidean measure for the distance calculus, each cluster is approached by a spherical distribution.

The FCM algorithm minimizes an objective function that depends on a set of prototypes v_j directly related to a given number of c clusters, and the distance of the prototypes to the whole set of patterns x_i . Consider a set of n unlabeled patterns or data points $X = \{x_1, x_2, \dots, x_n\}$ in a p dimensional

space, that is, $x_1 \in R^p$, where p represents the dimension and each dimension represents a feature of the patterns. Based on the Euclidean distance, the objective function of the FCM algorithm to be minimized is

$$J_m(U, V) = \sum_{j=1}^c \sum_{i=1}^n (\mu_{ij})^m d_{ij}^2 \quad (3)$$

where U is the matrix of membership values whose elements are μ_{ij} , which represents the membership value of the i^{th} pattern to the j^{th} cluster, V is the vector of prototypes, $d_{ij}^2 = \|x_i - v_j^{(k)}\|_2$ is the Euclidean norm where $v_j^{(k)}$ corresponds to the prototype of the cluster j^{th} at iteration k and, finally, $m \in (0, +\infty)$ is a parameter that controls the fuzziness, usually $m = 2$. The membership values, however, have to satisfy the following constraints: $\mu_{ij} \in [0, 1], i = 1, 2, \dots, n, j = 1, 2, \dots, c, \sum_{j=1}^c \mu_{ij} = 1, i = 1, 2, \dots, n$ and $0 < \sum_{i=1}^n \mu_{ij} < n, j = 1, 2, \dots, c$, and induces a fuzzy partition, represented by the matrix M_{fc} of dimension $(c \times n)$, and given by

$$M_{fc} = \{U \in R^{c \times n} | \mu_{ij} \in [0, 1], \forall i, j; \sum_{j=1}^c \mu_{ij} = 1, \forall j = 1, c; 0 < \sum_{i=1}^n \mu_{ij} < n, \forall i = 1, n\} \quad (4)$$

By using the Lagrange multiplier technique, the previous problem can be solved as an unconstrained optimization problem that conducts to the following expressions when minimized with respect to the prototypes and to

the membership values, respectively,

$$\mu_{ij}^k = \frac{1}{\sum_{k=1}^c \left(\frac{d_{ij}}{d_{ik}}\right)^{\frac{2}{m-1}}}, i = 1, 2, \dots, n, j = k = 1, 2, \dots, c \quad (5)$$

$$v_j^k = \frac{\sum_{i=1}^n (\mu_{ij}^{(k-1)})^m x_i}{\sum_{i=1}^n (\mu_{ij}^{(k-1)})^m}, j = 1, 2, \dots, c \quad (6)$$

According to [24], half of the FCM applications are on image analysis.

Thresholding is the most used technique for the image segmentation based on grey values corresponding to the objects of interest and the background. The purpose of using the method is to find an appropriate threshold (*th*) to separate an object of interest from another. When there are only an object and the background, the result is a binary image where pixels with grey values greater than the threshold represent the object, and the remaining pixels are associated to the background, or vice versa. When it is necessary to identify more than two objects, that is, $\{C_1, C_2 \dots C_K\}$, where K represents the number of classes or objects, a threshold has to be identified to establish the division between each pair of objects, what is known as multi-level thresholding. The thresholding methods are non-parametric algorithms as they use variance, entropy and minimal error as criteria for classification and validation on the threshold quality.

The Otsu's method [5] is one of the most popular algorithms based on the histogram thresholding, as it allows the calculus of an optimum threshold

through the variance maximization between classes. This method has been used across a wide range of different research fields. For example, for the segmentation of medical images; as those of the brain or MRI [25] for the lung [26], for microcalcifications in mammograms [27], or for the segmentation of soil images [28], [29], [30], [31].

The Otsu's method [13] is a non-parametric procedure that finds an optimal threshold by the variance maximization between-classes in a sweep of the whole space of grey values and considering as criterion the weighted sum of variances, that maximizes the separation between cluster means [17]. In that way, there is no need for previous information about the image to be segmented. According to the principle of operation, the Otsu method works well with images that have a bi-modal histogram for the image segmentation in two classes, something quite common in soil images. Therefore, for a digital 1-D image I represented in L grey levels, that is the set $\{0, 1, 2, \dots, L - 1\}$, the histogram can be built using the frequency of grey values according to the color of the pixels. In other words, $H = \{f_0, f_1, \dots, f_{(L-1)}\}$, where f_i denotes the number of pixels with gray level i whereas $N = f_0 + f_1 + \dots + f_{i(L-1)}$ represents the total number of pixels in the image. However, the method is based on the occurrence probability that, for the i^{th} grey level, is given by $p_i = f_i/N, p_i \geq 0$ and $\sum_{(i=0)}^{(L-1)} p_i = 1$.

For the segmentation of K groups or classes $\{C_1, C_2, \dots, C_K\}$, the Otsu method has to find $(k - 1)$ thresholds, that is $T = \{t_1, t_2, \dots, t_{K-1}\}$, keeping an order relation $t_1 < t_2 < \dots < t_{K-1}$ and $t_i \in (0, L - 1), i = 1, \dots, K - 1$.

For each cluster C_k , the cumulative probability w_k and the mean grey value μ_k are given by:

$$w_k = \sum_{i \in C_k} p_i \quad (7)$$

$$\mu_k = \sum_{i \in C_k} \frac{i \times p_i}{w_k}, k \in \{1, \dots, K\} \quad (8)$$

while the whole image mean intensity μ_T and the between-class variance σ_B^2 are given by

$$\mu_T = \sum_{k=1}^{K-1} w_k \times \mu_k = \sum_{i=0}^{L-1} i \times p_i \quad (9)$$

and

$$\sigma_B^2 = \sum_{k=1}^{K-1} w_k \times (\mu_k - \mu_T)^2 = \sum_{k=0}^{K-1} w_k \times \mu_k^2 - \mu_T^2 \quad (10)$$

Therefore, the optimal threshold values can be obtained by maximizing the between-class variance as follows:

$$(t_1^*, t_2^*, \dots, t_{K-1}^*) = \max \{ \sigma_B^2(t_1, t_2, \dots, t_{K-1}) \}, 0 < t_1 < t_2 \dots < t_{K-1} < L-1 \quad (11)$$

through the computation of the normalized histogram ($p_i, i = 0, 1, 2, \dots, L-1$) the cumulative sums $P_i(k) = \sum_{i=0}^k p_i$, the cumulative means $m(k) = \sum_{i=0}^k ip_i$ for $k = 0, 1, 2, \dots, L-1$, the global intensity mean, $m_g = \sum_{i=0}^{L-1} ip_i$ and the between-class variance $\sigma_B^2(k) = \frac{[m_G P_i(k) - m(k)]^2}{P_i(k)[1 - P_i(k)]}$.

2.4. Non-uniformity measures

The region non-uniformity measure can be applied to assess the quality of segmentation, even when the ground-truth information is not available [32], [33]. This criterion is calculated as:

$$NU = \frac{P}{T} \cdot \frac{\sigma_P^2}{\sigma^2} \quad (12)$$

where P represents the number of pixels of a pore, a solid or the gravel and T the totality of pixels in the segmented image, σ_P^2 and σ^2 are the variance of grey-scale values in the pore, solid and gravel space and total variance in the simulated greyscale image, respectively.

2.5. Procedure for the detection and quantification of the main elements in 2D CT soil images

The Fig. 6 presents a flow chart illustrating the methodology, and next there is a detailed description of the proposed methodology to identify pore, solid and gravel spaces and, for this work, using the standard clustering algorithms for the image segmentation.

- I. Selection of the total set of 2D images of the soil sample (with depth of 8 or 16 bits).
- II. Individual segmentation of the 2D images in three regions with the algorithms: k-Means, Fuzzy c-Means and Otsu multilevel method.

- III. Generation of the binary images for each of the three identified regions (pores, solids and gravel).
- IV. Calculus of the statistical parameters (number and percentage of pores and solids, mean value for each region, etc.) for each 2D image.
- V. Calculus of the NU values for each segmented region (pore, solid and gravel) in each individual 2D image.
- VI. Evaluation of the segmentation quality based on the NU values; the closer the NU values to zero, the better the segmentation results.
- VII. With the set of binary images for the pores and the solids, stack them in the corresponding order such that the 3D reconstruction is possible.
- VIII. Interpolation between each pair of consecutive 2D binary images allows completing the 3D approximation of the pore and solid structures of the soil simple.

3. Computational results and analysis

3.1. Segmentation

Due to the great similarity of results with the three methods, k-Means, FCM and Otsu, only the segmentation results of the FCM are included in Fig. 7. However, the graphics for the non-uniformity values, the number of pores and solids, the percentage of pores, solids and gravel, as well as the number of pores and solids by size are given below, where the differences among the results can be evaluated. The segmentation results of four original images

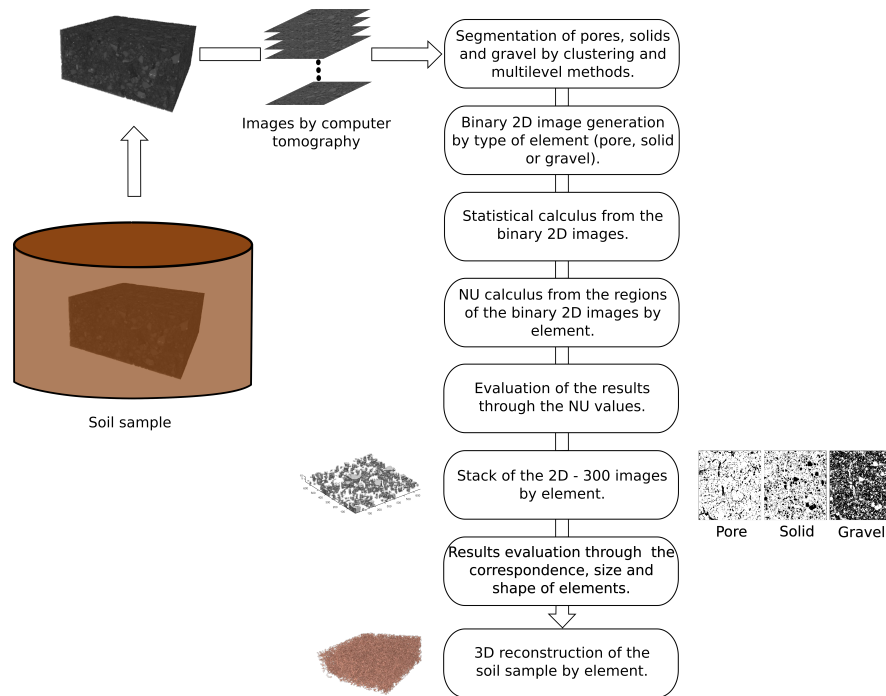


Figure 6: Flow chart that illustrates the detection and quantification methodology of pore, solid and gravel spaces in 3D CT real soil samples.

with the FCM algorithm in three regions (pore, solid and gravel spaces) are shown in Fig. 7. The first column (Fig. 7(a, e, i and m)) contains the original images, the second column (Fig. 7(b, f, j and n)) the binary images of the pores represented in black color, the third column (Fig. 7(c, g, k and o)) the binary images of the solids in black color and the fourth column (Fig. 7(d, h, l and p)) the binary images of the gravel in black color. In order to have a more quantitative estimation on the quality of the segmentation results, the NU measure was applied to every object of interest in every 2D image of the total set of 300 images of the soil sample using the three segmentation methods (k-Means, FCM and Otsu). The results are presented according to

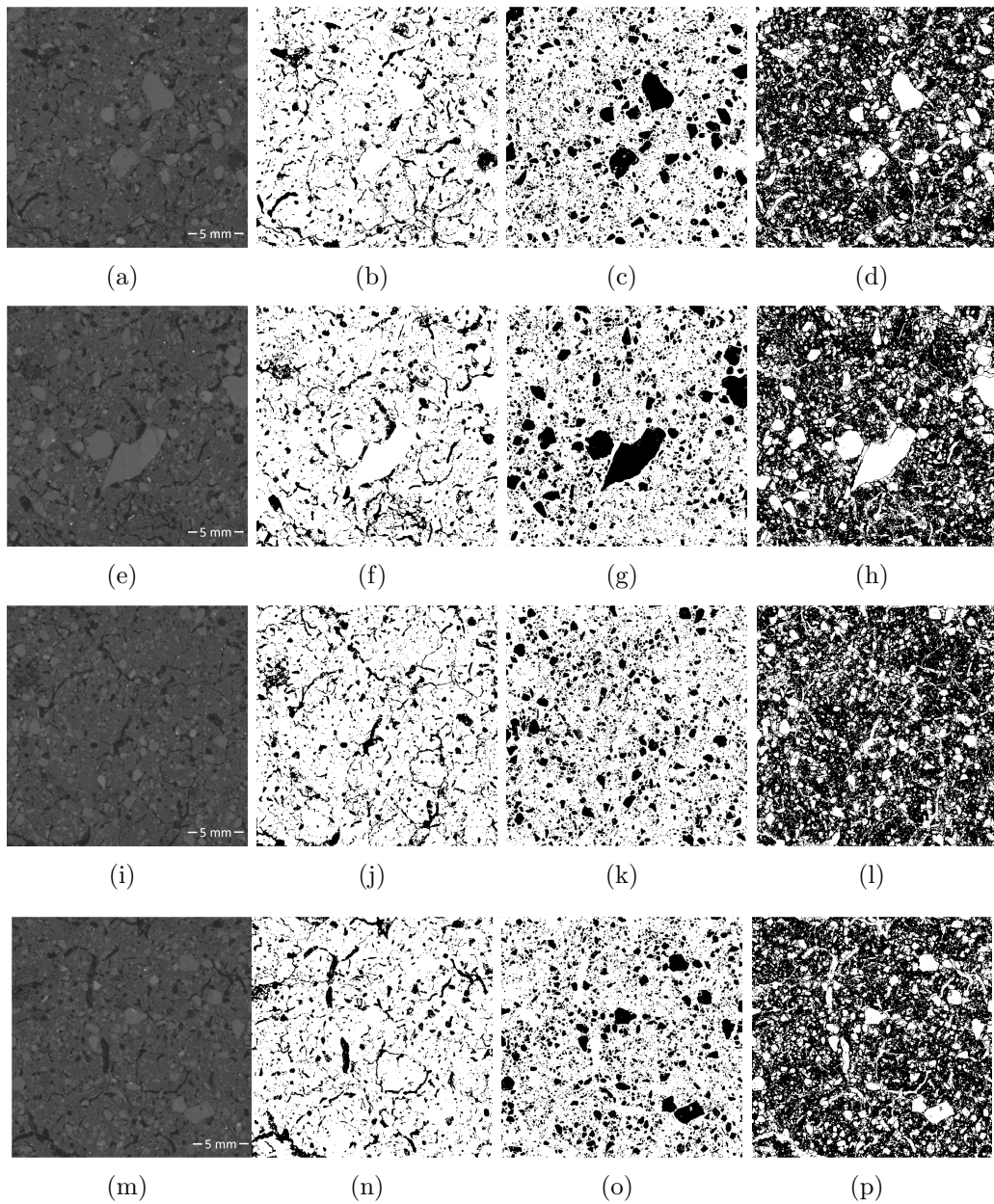


Figure 7: Original images with depth of 16 bits (a) Im_000, (e) Im_001, (i) Im_002, (m) Im_299. Binary images segmented with the FCM algorithm: (b, f, j, n) pore spaces represented in black color, (c, g, k, o) solid spaces represented in black color, (d, h, l, p) gravel represented in black color.

the depth of the image. Therefore, Fig. 8 contains the results for the images with a depth of 8 bits, whereas Fig. 9 contains the results for a depth of 16 bits. In these images the NU values of each object of interest (pores, solids and gravel) are plotted independently.

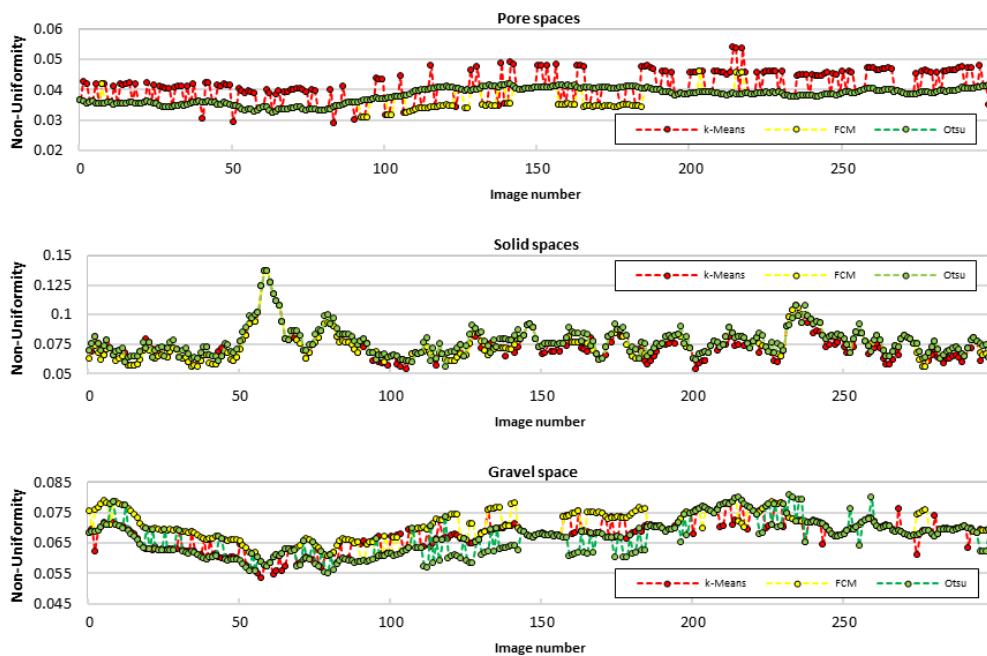


Figure 8: NU values corresponding to the objects of interest (pores, solids and gravel) in each one of the 300 images of the soil sample with depth of 8 bits.

As can be observed in Fig. 8 and Fig. 9, the NU values for the three objects of interest are very close to zero, that is, only in a few cases for the solids does the NU values exceed 0.1. Although the results for the depth of 8 bits show a greater variation, they are still very small and with NU values comparable

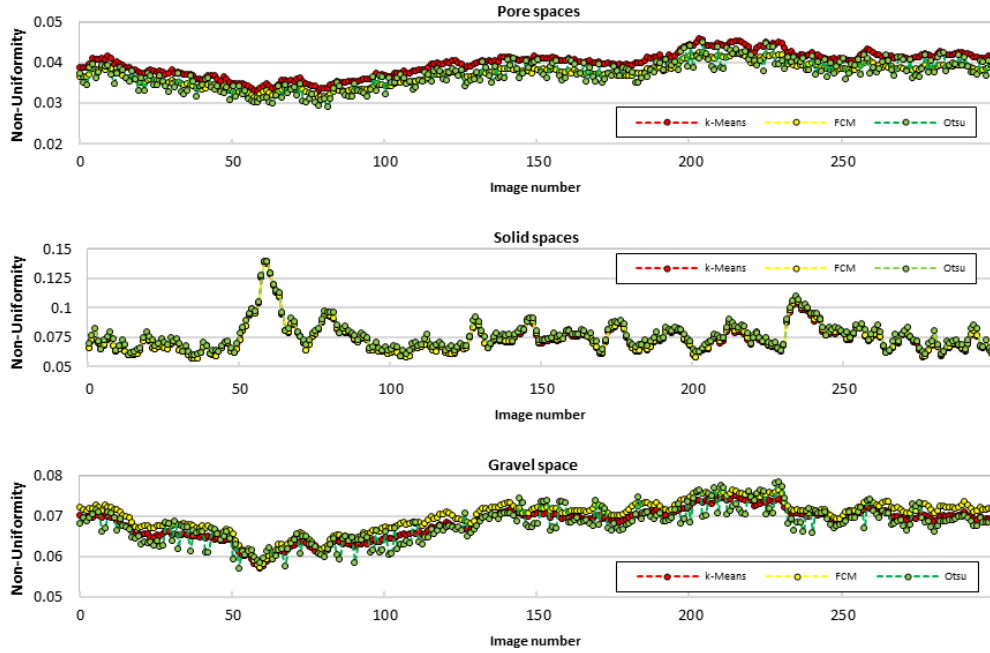


Figure 9: NU values corresponding to the objects of interest (pores, solids and gravel) in each one of the 300 images of the soil sample with depth of 16 bits.

to those of the depth of 16 bits. That means that the segmented regions are very homogeneous with the lowest and more stable values for the pore spaces, so these are the most homogeneous regions with NU values ranging between 0.03 and 0.05. The NU values for the solid spaces are less stable and present some peaks, the higher one located between the images 50 and 70. This phenomenon is explained by the fact that there exist several white solid spaces in the original images that clearly differs from the rest, and this reduces the homogeneity of the segmented regions of solids.

According to the results in Fig. 8, the calculated NU values for the three

segmentation methods are very close, with more important variations in some images for the k-Means and Otsu methods, even though the NU values are very low in all cases. These results are closer for the three methods in the totality of images with 16 bits depth with the exception of the k-Means for the pore spaces that gives globally higher values. On the other hand, the NU values for the results regarding the pores and the gravel with depth of 16 bits show some correlation, as can be seen in Fig. 9.

3.2. Number of pores and solids

Once the pore, solid and gravel spaces were identified in the 300-2D images and their homogeneity was through the NU values, with very good results as shown in Fig. 8 and Fig. 9, the pores and solids were counted in every single 2D image and the results are plotted in Fig. 10 for the images with depth of 8 bits and in Fig. 11 for a depth of 16 bits. In this last case the results are very similar as can be appreciated in the graphs. On the other hand, the results for the images with depth of 8 bits are more variable but with comparatively close values. For the 2D images with depth of 16 bits, the number of pores ranges approximately from 2100 to 3100, and the number of solids from 3600 to 5000, as can be seen in Fig. 11. The graphs of the results using the different methods are very close, so they can be considered similar. On the other hand, the reduction on precision by reduction on the depth from 16 to 8 bits of the 2D images, results in an increase of variations on the quantifications of the number of elements. See Fig. 10. This is a

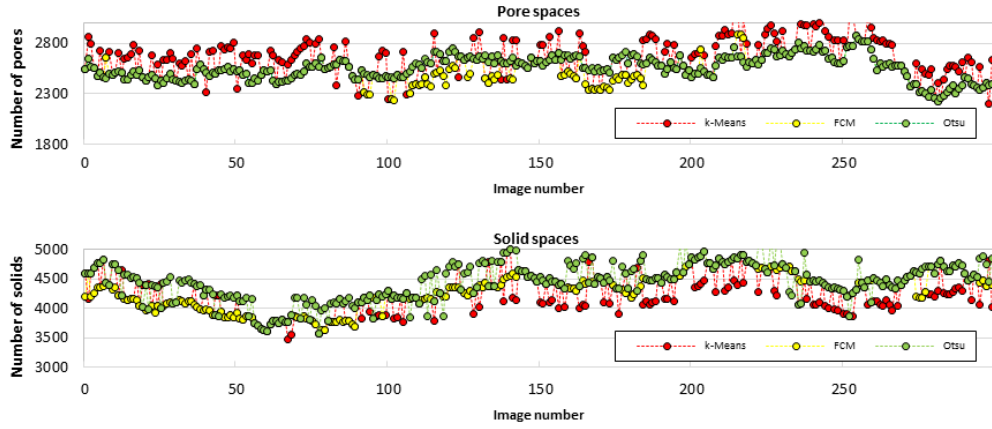


Figure 10: Total number of pores and solids in each individual 2D image of the soil sample with depth of 8 bits.

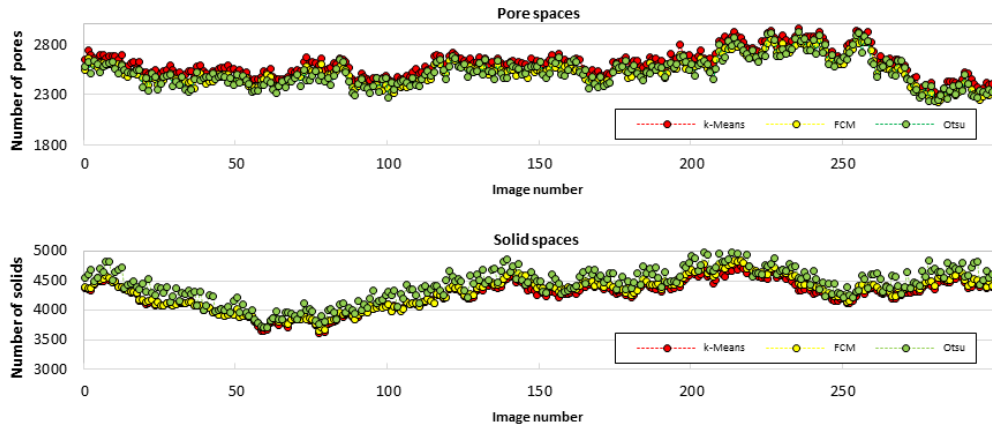


Figure 11: Total number of pores and solids in each individual 2D image of the soil sample with depth of 16 bits.

consequence of the loss of micropores due to the thicker discretization, on the one hand, and the separation of the pores due to the discretization of the intermediate gray levels in some pores, on the other hand.

3.3. Size of pores and solids

Simultaneously to the identification of the pores and solids, the number of pixels of each object was determined so its corresponding size could be calculated. Due to the great quantity of objects and variations in size, these were divided in three groups as shown in Fig. 12 to Fig. 15. The corresponding groups are pores or solids represented by: one pixel, two to 100 pixels and more than 100 pixels. Besides, these are divided by the depth of the images, that is, for 8 bits or 16 bits. Observing Fig. 12 and Fig. 13, the number

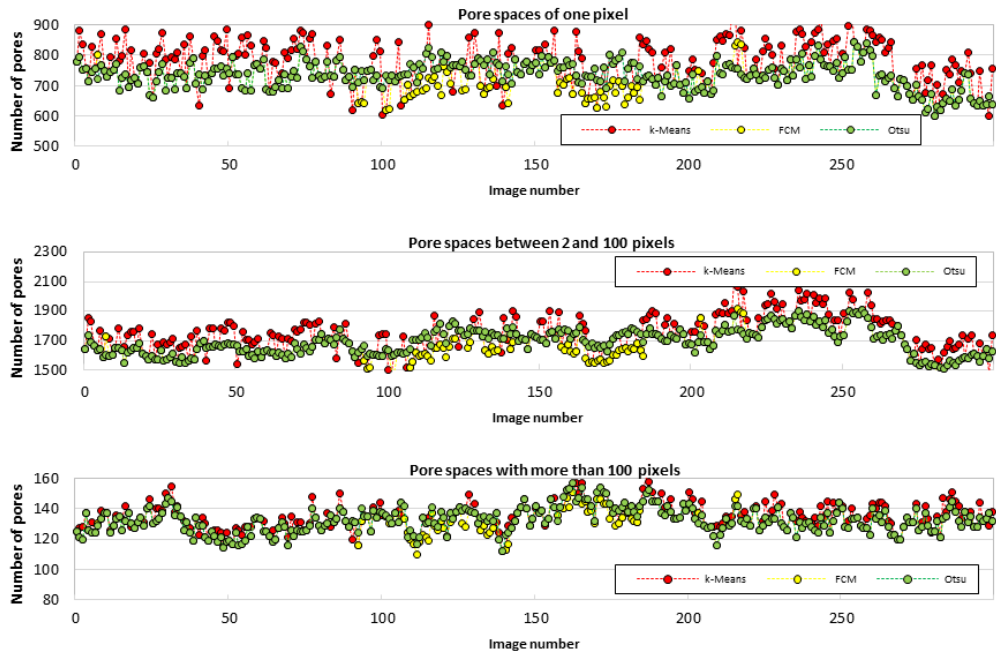


Figure 12: Total number of pores with size: a) of one pixel, b) $1 < pixels \leq 100$, and c) $100 < pixels$ (images with depth of 8 bits).

of pores of one-pixel size varies between 580 and 900, the number of pores

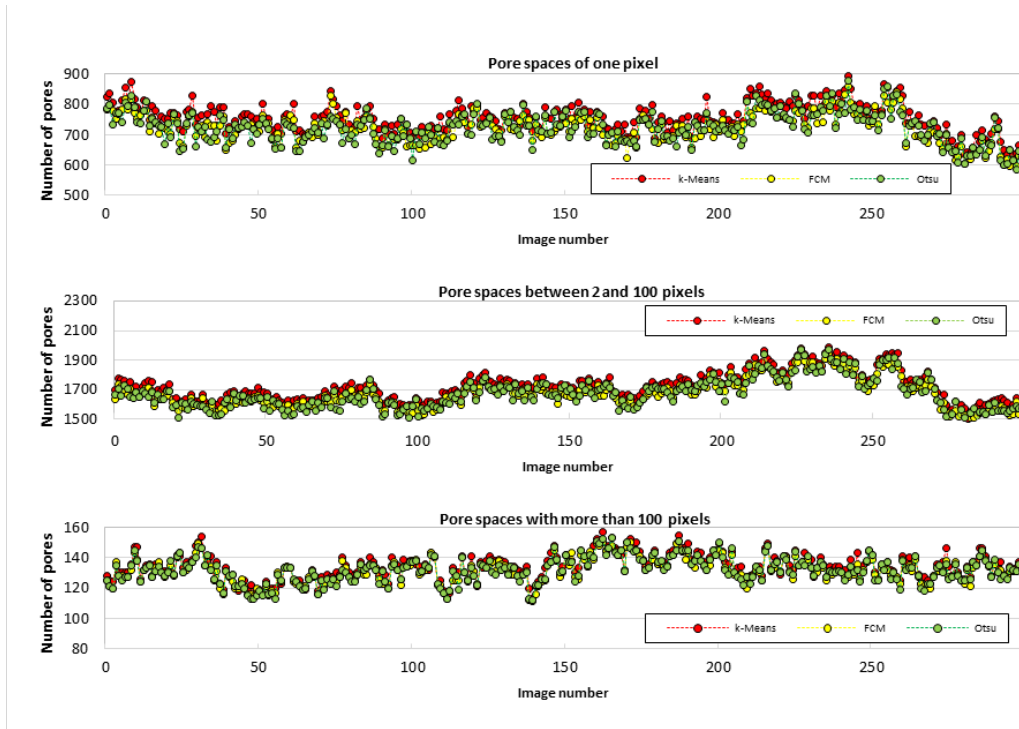


Figure 13: Total number of pores with size: a) of one pixel, b) $1 < pixels \leq 100$, and c) $100 < pixels$ (images with depth of 16 bits).

of intermediate size varies from 1500 to 2100 and the bigger ones between 110 and 160. Generally, more small and medium pores were identified with the k-Means, whereas the FCM and the Otsu methods gave similar results. Besides, the results were more dispersed when the 2D images with 8 bits depth were used, which is in agreement with the division of some pores due to the discretization in a smaller number of grey values.

Similarly, the number of solids are given by size in Fig. 14 and Fig. 15. As with the pores, the solids were divided in three groups corresponding to objects of one pixel, two to 100 pixels and more than 100 pixels. The number

of smallest solids vary between 880 and 1400, the quantity of medium solids between 2500 and 3600 and the number of bigger solids between 160 and 225. In general, the k-Means and the Otsu method presented larger variations.

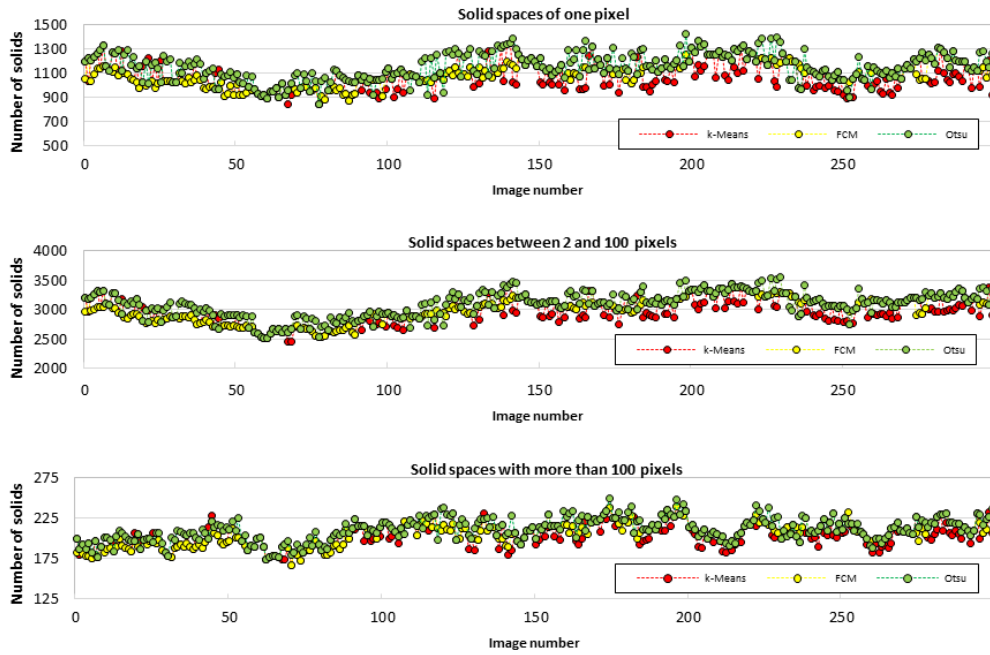


Figure 14: Total number of solids with size: a) of one pixel, b) $1 < pixels \leq 100$, and c) $100 < pixels$ (images with depth of 8 bits).

3.4. Quantification of pore, solid and gravel spaces

Once the number of pores and solids, as well as their sizes were available, it was possible to determine their corresponding percentage in each 2D image. The corresponding results are plotted for each individual 2D image in Fig. 16 and Fig. 17 for a depth of 8 and 16 bits respectively. According to these results, the percentage of pores varies between 14 and 17%, the percentage

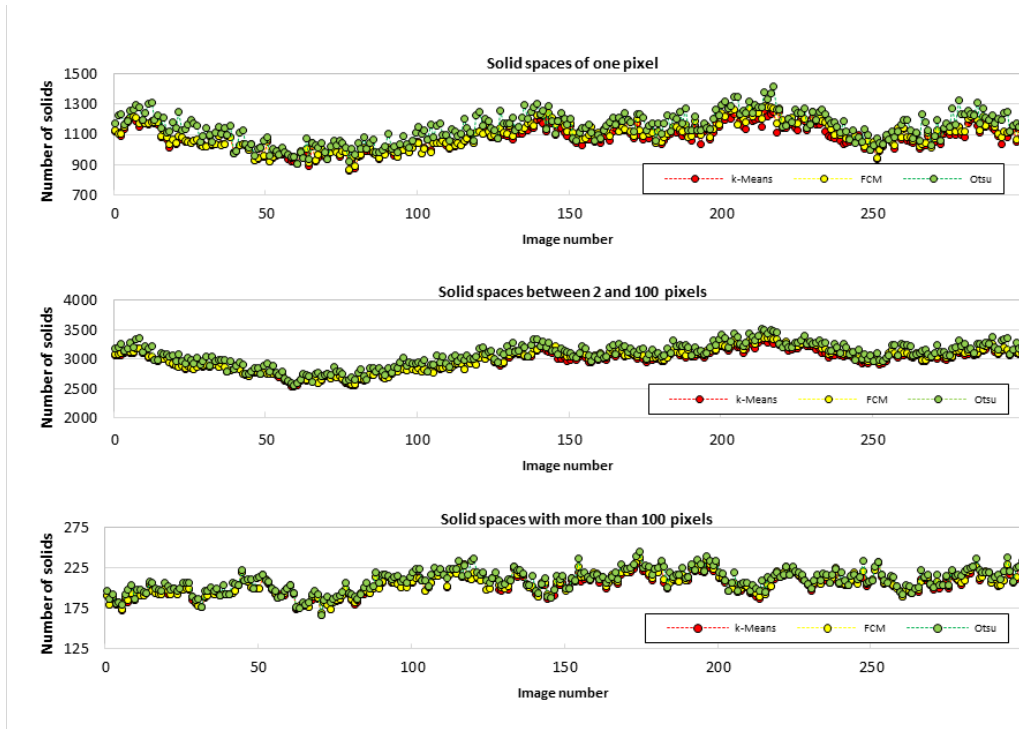


Figure 15: Total number of solids with size: a) of one pixel, b) $1 < pixels \leq 100$, and c) $100 < pixels$ (images with depth of 16 bits).

of solids between 20 and 32% and the gravel space between 53 and 64%. These results show the homogeneity in the soil studied. Besides, the graphs of solids and gravel of Fig. 16 and Fig. 17 show an inverse correlation, which means that as the solids increases within an image, the gravel reduces and vice versa. This result is independent on the depth of the grey level and the segmentation method, although the results for a depth of 16 bits are more clearly defined.

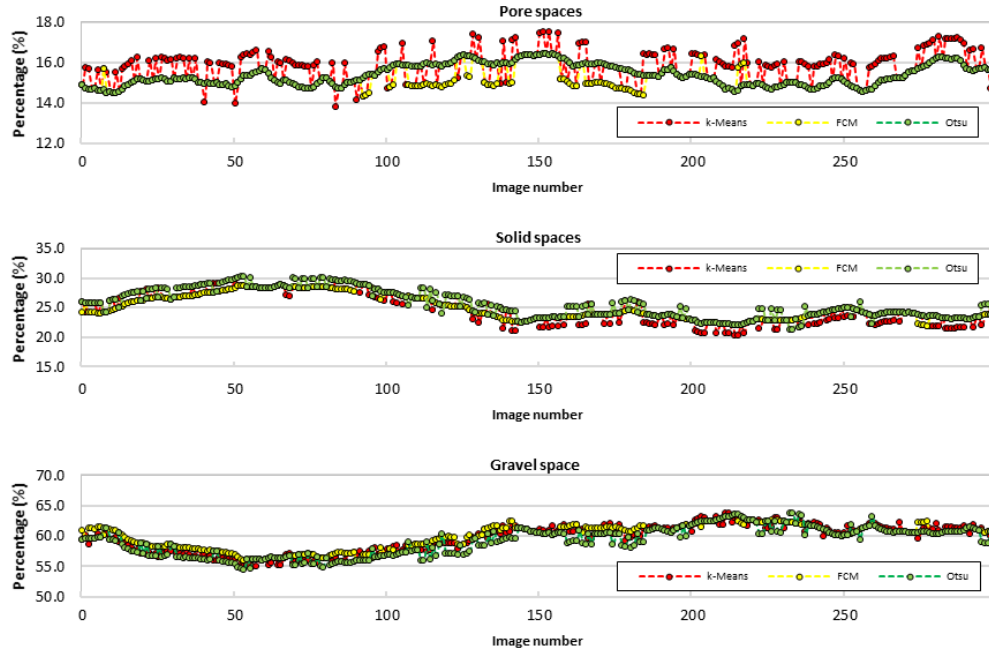


Figure 16: Percentage of pores, solids and gravel according to the segmentation process in images with depth of 8 bits.

3.5. Quantification of results with global data

In order to evaluate how close the results were obtained with the k-Means, FCM and Otsu methods, in this section we analyze the number of elements and their uncertainty, the magnitude of errors when comparing the segmentation methods and the global percentages. This analysis includes the reduction on the depth of the 2D images from 16 to 8 bits. As can be observed in Table 1, the number of pores remains very stable no matter the method or the depth of the images. The reduction on the depth affected the results of the k-Means although it improved the results of the FCM and Otsu methods.

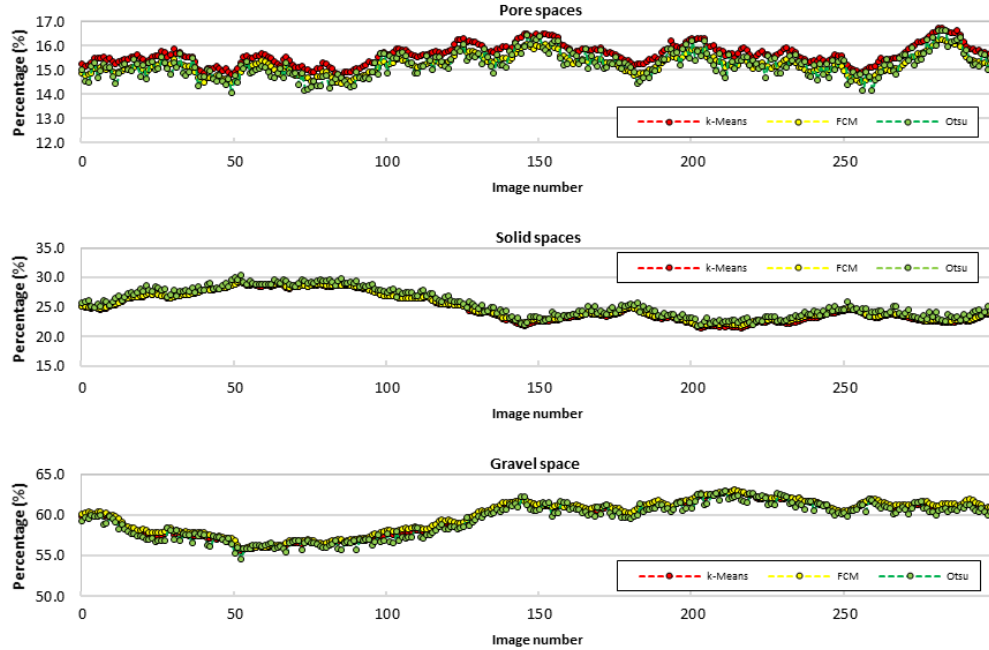


Figure 17: Percentage of pores, solids and gravel according to the segmentation process in images with depth of 16 bits.

This stability is also observed when considering the mean number of solid spaces independently of the segmentation method or the depth. However, for the solid spaces there is a loss in precision about 2.2% in average, and this is the most important loss identified resulting from the reduction of the depth of the 2D images. The uncertainties reported in Table 1 are the result of image processing, as well as the variation of the elements through the total set of images. This can be seen in Fig. 14 and Fig. 15, or even in Fig. 18 where there are pores that begin, or end, in the first or last image, or pores only present in some intermediate images.

Algorithm \ depth	Pores		Solid	
	16 bits	8bits	16 bits	8 Bits
k-means	2606 \pm 10.2%	2642 \pm 13.4%	4256 \pm 11.6%	4239 \pm 14.6%
FCM	2526 \pm 10.5%	2527 \pm 10.1%	4302 \pm 12.3%	4308 \pm 14.2%
Otsu	2527 \pm 11.1%	2559 \pm 09.0%	4427 \pm 12.8%	4444 \pm 14.4%

Table 1: Mean number of pores and solids and their uncertainty according to the segmentation method in the 300-2D images.

In Table 2 there are the relative errors when comparing the k-Means and the Otsu methods against the FCM. According to the results, the FCM and the Otsu methods got very similar results for the pores and the k-Means results were further away. A different situation occurred with the solids as the k-Means gave closer results to the FCM and the results of the Otsu method were more distant. Therefore, the values of Table 2 suggest that the better algorithm from those reported there for the identification of pores and solids is the FCM, since in both cases there is another algorithm that supports it with very similar results.

Algorithm \ depth	Pores		Solid	
	16 bits	8bits	16 bits	8 Bits
k-means	3.11	4.35	1.8	1.63
Otsu	0.04	1.25	2.82	3.06

Table 2: Global errors of the k-Means and Otsu methods regarding the FCM method.

The mean percentages of pore, solid and gravel spaces are reported in Table 3 where there is a great agreement between the methods that are not affected by the reduction on the depth of the 2D images.

Due to the type of soil, which has a very homogeneous structure, it has been

Algorithm \ depth	Pores		Solid		Gravel	
	16 bits	8bits	16 bits	8 Bits	16 bits	8 Bits
k-means	15.62	15.77	24.73	24.67	59.65	59.56
FCM	15.20	15.20	24.91	24.93	59.89	59.87
Otsu	15.21	15.37	25.43	25.51	59.36	59.12

Table 3: Mean percentage of pores, solids and gravel according to the segmentation method applied to the 300-2D images.

identified with three standard algorithms based on two different segmentation criteria, obtaining very similar results. However, less homogeneous soil images may require preprocessing, which induces some loss of information, the use of more sophisticated and robust segmentation algorithms, or even the improvement of some existing algorithms with which we can determine the particularities of the type of soils or samples. As the homogeneity decreases, the quality of the results also decreases. This explains why there are many published works only dealing with the pores identification, and until recently the interest arose to identify more elements in samples in order to better characterize the soils.

3.6. 3D reconstruction of the identified pore spaces within the soil sample

Given the difficulty to differentiate the segmentation results of pores, solids and gravel through the 2D images, as the k-Means, FCM and Otsu methods gave very close results; in this section, we include 3D reconstruction of the pores and solids. Initially, in Fig. 18, we included the larger pores and solids found in 10 consecutive images and using the k-Means algorithm, the simplest one. The purpose of this reconstruction is to evaluate the size, shape and continuity of pores and solids in the set of images. The great

coincidence of the objects through the images contribute to the validation of the results. The Fig. 18a shows the continuity of pores in the 10 images with depth of 16 bits, whereas Fig. 18b the continuity of solids.

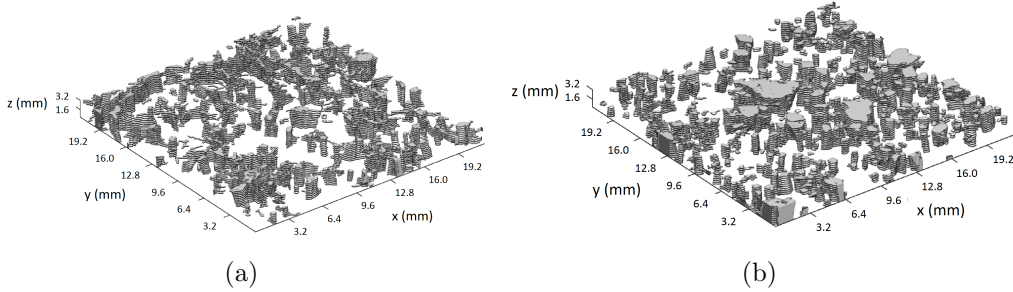


Figure 18: Stack of 10-2D images segmented with the k-Means algorithm. (a) Pores with size superior to 100 pixels. (b) Solids with size superior to 100 pixels.

After a partial evaluation of the pores and solids in a 3D reconstruction, the totality of results corresponding to the pores and solids were used to approximate the total soil sample. Therefore, Fig. 19 contains the approximation of the pores but divided in two groups for a better appreciation, one group containing the pores with sizes no greater than 100 pixels (equivalent to 320 microns), which is represented in Fig. 19a. The other group corresponding to the pores with more than 100 pixels and represented in Fig. 19c. Both images also include the corresponding 3D orthoslice, which allows us to have an interior view of the 3D reconstruction of the sample and where the pores can also be evaluated qualitatively. The total 3D reconstructions are based on the FCM segmentation results and images with depth of 16 bits.

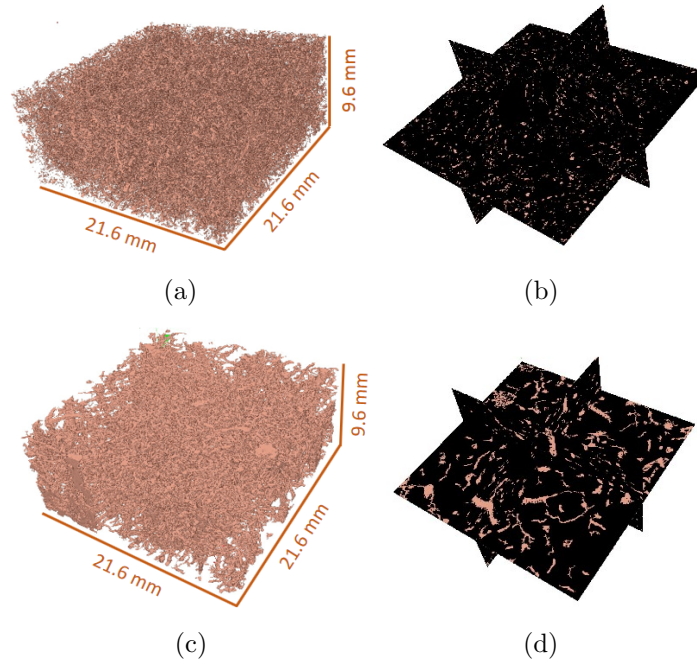


Figure 19: Image of the 3D reconstruction of the porosity using the FCM clustering algorithm and depth of 16 bits. (a) Pores smaller or equal to 100 pixels and (b) 3D orthoslice, (c) pores greater than 100 pixels and (d) 3D orthoslice.

A similar reconstruction was made for the solids. The results are provided in Fig. 20 where the solids were also divided in two groups according to their size, so solids with 100 pixels or less are represented in the 3D approximation of Fig. 20a, and solids with size superior to 100 pixels in Fig. 20b. By a comparative analysis with the Fig. 19 results, the solids have a more regular form and are also more isolated than the pores since there is almost no connection between them. The orthoslices also provide an internal view of the 3D sample and allow a qualitative evaluation of the solids.

The correspondence and continuity of pores and solids through the 2D images

can be seen as a qualitative criterion to evaluate the results and we can say that they were correctly identified. Besides, the stability of the results through the 300 images is an indication that the composition remains with little changes within the whole soil sample.

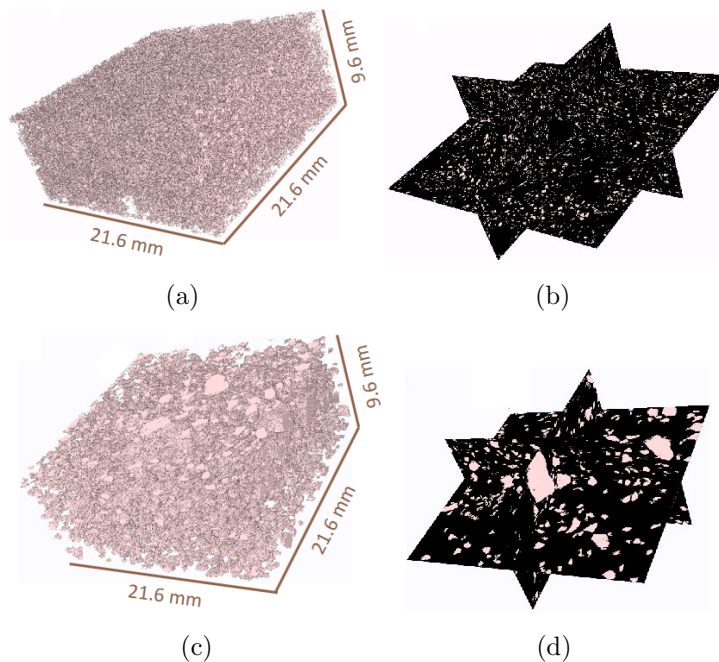


Figure 20: Image of the 3D reconstruction of the solids using the FCM clustering algorithm and depth of 16 bits. (a) Pores smaller or equal to 100 pixels and (b) 3D orthoslice, (c) pores greater than 100 pixels and (d) 3D orthoslice.

4. Conclusions

According to the results, the pore, solid and gravel spaces were very well identified by the k-Means, FCM and Otsu methods, as the corresponding NU values were, most of them, inferior to 0.1, which corresponds to very homogeneous groups identified in each 2D image of the 300 set of the soil sample.

Therefore, the size, geometry and connectivity of the objects between two consecutive 2D images have a great correspondence, and this is clearly observed through the 3D reconstruction of the soil sample from the total set of 2D binary images representing the pores and the solids. Besides, this representation allows visualization of the distribution of pores and solids such that the porous and solid structures can easily be evaluated. Consequently, the homogeneity of objects also helped the segmentation process, which has been examined by three methods in this work providing similar results, especially for the macro pores and solids, although there are some relative differences when comparing micro and medium pores and solids, particularly with the micro pores reaching a difference approximate of 2.2%. These micro pores and solids (objects of a pixel) will be analyzed more thoroughly in the future to know what they are: pores, solids or noise.

Additionally, the depth of the original 2D images was reduced from 16 bits to 8 bits and the same test were performed resulting comparable object classification and NU values, with objects very well segmented and with very homogeneous features. In both cases of pixel's depth, the segmentation methods were applied directly to the original 2D images, and the most notorious differences were related to micro and medium pores, as there was some loss of information, showing a size variation between 0 and 8%. On the other hand, the macro pores and solid space remained practically unchanged keeping the same size, or the same number of pixels. Similarly, we attribute this result to the kind of soil and the high quality of the images where a depth of 8 bits and

the simplest clustering algorithm, as the k-Means, worked very well. Finally, as the imaging technology advances, X-ray CT in this case, it is likely that there will be enhanced imaged quality and phase contrast allowing a greater possibility of better structure/feature definition and, therefore, an increasing on the number of very well identified objects in soil samples.

Acknowledgment

The authors wish to thank the The National Council for Science and Technology (CONACyT) in Mexico. Part of this work was supported for the incorporation of new teachers UDG-PTC-1461 SEP program. We are grateful to the Comunidad de Madrid (Spain) and Structural Funds 2014-2020 (ERDF and ESF) for the financial support (project AGRISOST-CM S2018/BAA-4330).

References

- [1] H. J. Vogel, A numerical experiment on pore size, pore connectivity, water retention, permeability, and solute transport using network models, *European Journal of Soil Science* 51 (2000) 99–105.
- [2] M. L. Rockhold, R. R. Yarwood, J. S. Selker, Coupled microbial and transport processes in soils, *Vadose Zone Journal* 3 (2004) 368–383.
- [3] I. Young, J. Crawford, N. Nunan, W. Otten, A. Spiers, Chapter 4

- microbial distribution in soils: Physics and scaling, in: *Advances in Agronomy*, volume 100, Academic Press, 2008, pp. 81–121.
- [4] J. M. Blair, R. E. Falconer, R. E. Milne, I. M. Young, J. W. Crawford, Modeling three-dimensional microstructure in heterogeneous media, *Soil Science Society of America Journal* 71 (2007) 1807–1812.
- [5] R. Pajor, R. Falconer, S. Hapca, W. Otten, Modelling and quantifying the effect of heterogeneity in soil physical conditions on fungal growth, *Biogeosciences* 7 (2010) 3731–3740.
- [6] A. Kravchenko, R. E. Falconer, D. Grinev, W. Otten, Fungal colonization in soils with different management histories: modeling growth in three-dimensional pore volumes, *Ecological Applications* 21 (2011) 1202–1210.
- [7] F. Dullien, *Porous Media: Fluid Transport and Pore Structure*, 2nd. ed., Academic Press, Inc, New York, 2012.
- [8] T. Elliot, R. Heck, A comparison of 2d vs. 3d thresholding of x-ray ct imagery, *Canadian journal of soil science* 87 (2007) 405–412.
- [9] R. M. Haralick, L. G. Shapiro, Image segmentation techniques, *Computer Vision, Graphics, and Image Processing* 29 (1985) 100 – 132.
- [10] N. R. Pal, S. K. Pal, A review on image segmentation techniques, *Pattern Recognition* 26 (1993) 1277 – 1294.

- [11] D. L. Pham, C. Xu, J. L. Prince, Current methods in medical image segmentation, *Annual Review of Biomedical Engineering* 2 (2000) 315–337.
- [12] P. Baveye, W. Otten, A. Kravchenko, M. Balseiro-Romero, E. Beckers, M. Chalhoub, C. Darnault, T. Eickhorst, P. Garnier, S. Hapca, S. Kiranyaz, O. Monga, C. Mueller, N. Nunan, V. Pot, S. Schluter, H. Schmidt, H. Vogel, Emergent properties of microbial activity in heterogeneous soil microenvironments: Different research approaches are slowly converging, yet major challenges remain, *Frontiers in microbiology* 9 (2018) 1–48.
- [13] N. Otsu, A threshold selection method from gray-level histograms, *IEEE Transactions on Systems, Man, and Cybernetics* 9 (1979) 62–66.
- [14] M. Sezgin, B. Sankur, Survey over image thresholding techniques and quantitative performance evaluation, *Journal of Electronic Imaging* 13 (2004) 146 – 165.
- [15] N. Nunan, K. Ritz, M. Rivers, D. S. Feeney, I. M. Young, Investigating microbial micro-habitat structure using x-ray computed tomography, *Geoderma* 133 (2006) 398 – 407.
- [16] S. Arora, J. Acharya, A. Verma, P. K. Panigrahi, Multilevel thresholding for image segmentation through a fast statistical recursive algorithm, *Pattern Recognition Letters* 29 (2008) 119 – 125.

- [17] D.-Y. Huang, T.-W. Lin, W.-C. Hu, Automatic multilevel thresholding based on two-stage otsu's method with cluster determination by valley estimation, *International journal of innovative computing, information and control* 7 (2011) 5631–5644.
- [18] J. MacQueen, Some methods for classification and analysis of multivariate observations, in: *Proceedings of the fifth Berkeley symposium on mathematical statistics and probability*, volume 1, Oakland, CA, USA, 1967, pp. 281–297.
- [19] J. C. Bezdek, A primer on cluster analysis: 4 basic methods that (usually) work [book review], *IEEE Computational Intelligence Magazine* 12 (2017) 98–100.
- [20] E. Santolaria-Canales, Gumnet-guadarrama monitoring network. installation and set up of a high altitude monitoring network, north of madrid. spain, in: *EGU General Assembly Conference Abstracts*, volume 17, 2015.
- [21] T. Schmid, R. Incln-Cuartas, E. Santolaria-Canales, A. Saa, M. Rodriguez-Rastrero, L. Tanarro-Garcia, E. Luque, M. Pelayo, J. Ubeda, A. Tarquis, J. Diaz-Puente, J. D. Marcos, J. Rodriguez-Alonso, C. H. D., Palacios, J. Gallardo-Díaz, J. González-Rouco, Soil and geomorphological parameters to characterize natural environmental and human induced changes within the guadarrama range (central

- spain), in: EGU General Assembly Conference Abstracts, volume 18, 2016.
- [22] B. Ojeda-Magaa, J. Quintanilla-Domínguez, R. Ruelas, A. Tarquis, L. Gómez-Barba, D. Andina, Identification of pore spaces in 3d ct soil images using pfcM partitional clustering, *Geoderma* 217-218 (2014) 90 – 101.
- [23] R. O. Duda, P. E. Hart, D. G. Stork, *Pattern classification*, John Wiley & Sons, 2012.
- [24] J. Nayak, B. Naik, H. Behera, Fuzzy c-means (fcm) clustering algorithm: a decade review from 2000 to 2014, in: *Computational intelligence in data mining-volume 2*, volume 32, Springer, New Delhi, 2015, pp. 133–149.
- [25] S. Kotte, R. K. Pullakura, S. K. Injeti, Optimal multilevel thresholding selection for brain mri image segmentation based on adaptive wind driven optimization, *Measurement* 130 (2018) 340 – 361.
- [26] S. Uzelaltinbulat, B. Ugur, Lung tumor segmentation algorithm, *Procedia Computer Science* 120 (2017) 140 – 147.
- [27] M. A. Duarte, A. V. Alvarenga, C. M. Azevedo, A. F. C. Infantosi, W. C. A. Pereira, Automatic microcalcifications segmentation procedure based on otsu’s method and morphological filters, in: *2011 Pan American Health Care Exchanges*, 2011, pp. 102–106.

- [28] B. Ojeda-Magaa, J. Quintanilla Domínguez, R. Ruelas, J. J. Martín-Sotoca, A. M. Tarquis, Pore detection in 3-d ct soil samples through an improved sub-segmentation method, *European Journal of Soil Science* 70 (2019) 66–82.
- [29] S. M. Hapca, A. N. Houston, W. Otten, P. C. Baveye, New local thresholding method for soil images by minimizing grayscale intra-class variance, *Vadose Zone Journal* 12 (2013).
- [30] J. J. Martín-Sotoca, A. Saa-Requejo, J. Grau, A. Tarquis, Local 3d segmentation of soil pore space based on fractal properties using singularity maps, *Geoderma* 311 (2018) 175–188.
- [31] A. N. Houston, W. Otten, P. C. Baveye, S. Hapca, Adaptive-window indicator kriging: A thresholding method for computed tomography images of porous media, *Computers & geosciences* 54 (2013) 239–248.
- [32] Y. J. Zhang, A survey on evaluation methods for image segmentation, *Pattern recognition* 29 (1996) 1335–1346.
- [33] Y. J. Zhang, A review of recent evaluation methods for image segmentation, in: *Proceedings of the Sixth International Symposium on Signal Processing and its Applications* (Cat. No. 01EX467), volume 1, IEEE, 2001, pp. 148–151.